A numerical study of surface-wave-based tunnel detection at the Black Diamond Mines Regional Preserve, California

Christopher S. Sherman[1], James Rector[2], Douglas Dreger[3], and Steven Glaser[2]

[1] University of California Berkeley, Department of Civil and Environmental Engineering, Berkeley, California, USA and Computational Geosciences Group, Lawrence Livermore National Laboratory, Livermore, California, USA. E-mail: sherman27@llnl.gov.

[2] University of California Berkeley, Department of Civil and Environmental Engineering, Berkeley, California, USA. E-mail: jwrector@lbl.gov; glaser@berkeley.edu.

[3] Berkeley Seismological Laboratory, Berkeley, California, USA. E-mail: dreger@seismo.berkeley.edu.

ABSTRACT

Detecting underground voids, such as old mine workings, solution cavities in karst terrain, or unknown tunnels such as illicit cross-border tunnels, is a challenging problem for geophysics and an important concern for geotechnical design, public safety, and domestic security. Seismic surface-wave- based detection methods have become increasingly popular for detecting relatively shallow and small targets; however, the theoretical limitations of these methods have thus far remained unclear. We use a suite of 3D numerical simulations inspired by a tunnel detection experiment carried out at the Black Diamond Mines Regional Preserve (BDM) in northern California. The geophysical anomalies predicted by our numerical simulations at BDM agree with field observations, and our estimates for the location of the primary tunnel target agree with historical records in the area. Using our calibrated numerical model, we perform a parametric study to determine the effect of tunnel size, depth of burial, filling material, and source characteristics to determine the range over which surface-wave backscattering and attenuation-based methods are effective. In addition, we perform a regression analysis to determine a relationship for the maximum depth at which a tunnel may be detected via these approaches, given the target diameter, wavelength of interest, and the signal-to-noise ratio.

INTRODUCTION

Tunnel and underground void detection is an important, yet challenging problem in geophysics and engineering. It has important applications for the mining and transportation industries, public safety, and domestic security. These include determining the location of old abandoned mine workings, karst features, and covert tunnels. Because there is often no surface expression of these features, conventional methods for locating them are limited to costly and time-consuming exploration drilling. Over the past several decades, researchers have applied geophysical methods ranging

from gravity and resistivity to seismic diffraction in an attempt to identify voids. In many cases, these methods have been successful in determining the location of tunnels; however, the theoretical limitations of these methods remain poorly understood. In this paper, we conduct a numerical study of seismic surface-wave-based tunnel detection methods to explore their limitations with regard to tunnel depth, seismic wavelength, and heterogeneity. We also discuss a case study in tunnel detection at a site in the Black Diamond Mines Regional Preserve (BDM) near Antioch, California.

Background

In regions where the target void is large, shallow, and/or irregularly shaped (e.g., karst sinkholes), researchers favor potential-field geophysical methods such as microgravity and electrical resistivity (Butler, 1984; McCann et al., 1987; Rybakov et al., 2001; Van Schoor, 2002; Llopis et al., 2005; Kaufmann et al., 2011; Martínez-Moreno et al., 2013). The observed anomalies for these methods tend to be very small, often just above the survey resolution, and they tend to be more effective where the target is filled with water or air. Another significant challenge facing these methods is due to the significant smoothness requirements necessary for inversion, which smears out the effects of the already small anomalies (Riddle et al., 2010). Some researchers have reported success in locating similar large or irregular objects using low-frequency ground-penetrating radar (GPR) (Mochales et al., 2008). Because of the relatively high frequencies required to locate smaller objects and the highly attenuating materials in which they are located, signal degradation severely limits the usefulness of EM methods (Vesecky et al., 1980; Llopis et al., 2005).

A range of seismic-based geophysical methods has been applied in an attempt to locate subsurface voids. In comparison with gravity and resistivity, these are often more suitable for smaller objects with simpler geometry (e.g., tunnels). Body-wave diffraction imaging is often proposed for detecting voids, especially where the target is deeply buried (Belfer et al., 1998; Peterie et al., 2009; Sloan et al., 2010). In theory, this method should be capable of detecting a tunnel, regardless of its depth. However, because the tunnel diffraction is limited to relatively high frequencies, seismic skin depth is a severe limitation. In addition, reflections and scattering in the subsurface may easily obscure the target diffractions. The classic example for this application of diffraction imaging comes from U.S. military attempts to locate tunnels excavated in the Korean demilitarized zone (Vesecky et al., 1980). Their investigation concluded that the wavelength of the seismic waves required to detect the target tunnels is comparable with the average size of the local heterogeneities. As a result, they would require an unreasonably detailed model of the local geology for this method to be useful.

In regions where the goal is to detect clandestine tunnels as they are constructed (e.g., the US-Mexico border), researchers have proposed passive

seismic detection methods as an option (Llopis et al., 2005; Sabatier and Matalkah, 2008). The goal is to listen for seismic sources associated with excavation, which, depending upon their type and frequency, makes this method potentially powerful. One of the major challenges for passive detection methods is that they must reliably discriminate between tunnel construction noise and other nontrivial anthropogenic sources. In addition, these methods may require large static seismic arrays and significant resources for managing and processing the data they would produce.

Because the targets of interest are often very shallow, other body- wave-based methods, such as refraction or reflection, are not commonly applied due to surface waves interfering with the signals of interest. However, researchers have noted that in some cases indirect observations from these surveys may yield useful results. For instance, Belfer et al. (1998) and Sloan et al. (2013) find that by using refraction tomography, an apparent decrease in the raypath density may correspond to the target's location.

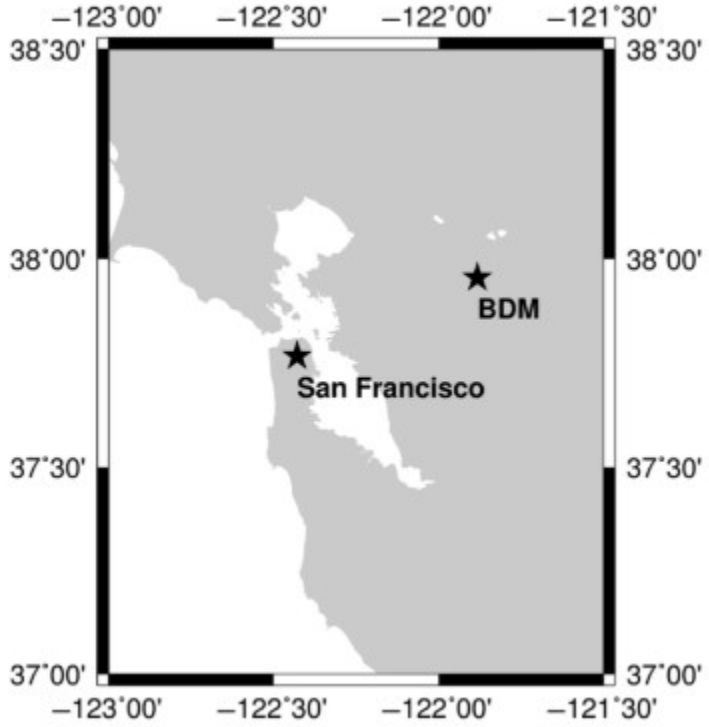

Figure 1. The location of the BDM test site.

Surface-wave void detection methods have several inherent advantages over body-wave diffraction: First, surface waves are generally the largest amplitude arrivals recorded on a surface array and are easy to generate using low-tech sources such as a sledge- hammer and plate. Second, surface-wave detection methods may rely on much lower frequencies, making them more resistant to the effects of near-surface heterogeneity. Third, using surface waves effectively limits the problem geometry to two dimensions, which significantly reduces the cost and complexity of

interpretation. Several field and numerical studies have reported success in locating shallow, man-made tunnels using surface-wave backscattering (Ivanov et al., 2003, 2016; Xia et al., 2007; Sloan et al., 2010, 2015; Morton et al., 2016) and surface-wave attenuation or multichannel analysis of surface waves (MASW) (Ivanov et al., 2003; Nasseri- Moghaddam et al., 2005; Putnam et al., 2009; Sloan et al., 2013). Korneev (2009) suggests a novel method for locating voids by identifying the emissions of Stoneley waves generated when a surface wave interacts with a fluid-filled void. This approach is advantageous because it relies on a very persistent signal and because the frequency content of the emitted wave may provide information regarding the size of the void in addition to its location.

Black Diamond Mines

BDM is named for its underground coal mining operations that began in the 1860s and continued through the early 20th century (see Figure 1). Beginning in the 1920s, the industry shifted toward underground silica sand mining, and later toward surface sand mining. In total, approximately 1.8 million tons of sand was mined at BDM until operations ceased in 1949. The East Bay Regional Park Service currently manages the land, and it has developed BDM into a mining museum.

There are several significant mining-related features at the site chosen for the tunnel detection case study, which are highlighted in historical records of the site (U.S. Department of the Interior, 1998). Our primary target was a very large 5.6 m diameter adit that is estimated to be at a depth of 6.2 m (measured to the center of the tunnel). The lateral location of this adit is well-constrained, and it is believed to be intact and filled with air. Our secondary target is a smaller 2.0 m diameter tunnel buried at a depth of approximately 24 m (again, measured to the center of the tunnel). The exact lateral location and the condition of this feature are unknown. The tunnel detection survey was conducted within an old surface sand mining excavation in the local Lower Domengine Formation (Sullivan and Sullivan, 2012), which has since been reclaimed for recreational use. In 1998, park officials noted a subsidence pit in the area, which was thought to be the result of a stopping failure related to a potential collapse of the lower tunnel. The pit was located to the south of the expected location of the tunnels, and has since been backfilled and grouted. A second, smaller subsidence feature appeared in 2012 and has since been filled in (J. McKanna, personal communication, 2013). A schematic showing the relation of these features to the field acquisition is included in Figure 2. We used a combination of surface-wave attenuation, surface-wave backscattering, and microgravity methods in an attempt to constrain the location of these features for the site operators.

METHODOLOGY

Void detection analysis

Surface-wave backscattering occurs when the wave interacts with the target and reflects back toward the seismic source. The location of the perceived source and the frequency content of the backscattered wavefield contain information regarding the location of the void along the seismic array and the depth of burial, respectively. In some cases, the backscattered waves are visible in the unprocessed seismic record; however, they are often obscured by the coda of the forward-propagating wavefield. Following the procedure set out by other investigators (Sloan et al., 2015; Ivanov et al., 2016), we isolate the backscattered waves by applying amplitude gain control (AGC), we apply a band-pass filter to individual traces to prevent spatial aliasing, and then we apply a directional *f*-*k* filter to remove the forward-propagating energy. Although an aggressive *f*-*k* filter may introduce some ripple effects into the processed results, the source of the backscattered wavefield is typically apparent in the processed record. As an optional step, we occasionally applied a normal moveout correction to field data and stack the results of multiple shots to further increase the signal-to-noise ratio of the backscattered wavefield. To compare the degree of backscattering between numerical simulations, we calculate the amplitude of the backscattered phase at a set distance back from the tunnel axis in which there is a visible separation from the direct phase.

In contrast to the backscattering analysis, the analysis of surface- wave attenuation is focused on variations in the amplitude of the wavefield because it passes over the target. In the case of a tunnel that extends a long distance in the out-of-plane direction and is buried at some depth less than the seismic wavelength of interest, we expect that, due to the superposition of the forward- and back- ward-propagating wavefields, the amplitude of the surface waves will be increased on the source side of the tunnel and decreased on the opposite side with respect to a shot in an equivalent tunnel- free medium (Xia et al., 2007). This is sometimes interpreted as a change in the apparent attenuation of the subsurface (Morton et al., 2016). In our analysis, we begin by applying a band-pass filter to the data and correcting for geometric spreading effects. Then, we

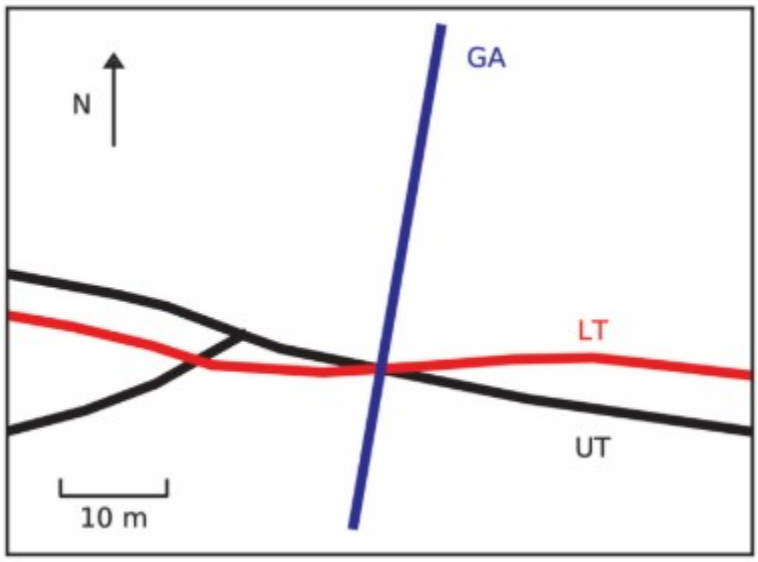

Figure 2. The expected location of the upper (UT) and lower (LT) tunnels, which are expected to be centered at depths of 6.2 and 24 m, respectively, and the GA at the BDM field site.

determine the envelope of the surface wavefield using the Hilbert transform and find the maximum value or total energy at each location E. Finally, we normalize these values against an arbitrary reference station and determine the deviation from the expected values for an equivalent tunnel-free system. For a tunnel buried in a homogeneous half-space, this is equivalent to equation 1:

$$S(x) = \frac{E_z(x)}{E_z(x_o)} \exp(\pi f(x - x_o)/QV_r) - 1, \qquad (1)$$

where S is the tunnel seismic anomaly, x is the distance of the recording station, x_o is the position of an arbitrary reference station on the source side of the tunnel, E_z is an estimate of the maximum amplitude or the total energy of the vertical component wavefield arriving at a given station, Q is the estimated attenuation quality factor for a tunnel-free system, and V_r is the surface-wave velocity. In this study, we determine the value of Ez at each station by calculating the Hilbert envelope function and integrating it over time, and we place the reference station at $x_o = 10$ m.

Numerical simulations

We use the massively parallel, 3D, elastodynamic finite-difference code E3D to simulate the behavior of the seismic wavefield as it interacts with a buried tunnel, and to explore the range of conditions in which surface-wave tunnel detection methods are viable. E3D is developed at Lawrence Livermore National Laboratory, uses a staggered grid formulation, is fourth-order accurate in space, is second-order accurate in time, and is capable of modeling regions with large contrasts in S-wave velocity. It has been applied to solve problems ranging from large-scale earthquake simulations to mod-

eling small-scale seismic surveys, and it is useful for modeling heterogeneous materials (Larsen and Grieger, 1998; Sherman et al., 2014).

The base configuration for our numerical simulations was inspired by the expected geometries and material properties at the BDM test site (see Figure 3). Each model domain is at least 60 m long, 45 m wide, and 45 m deep and has a grid size of 0.08 m.

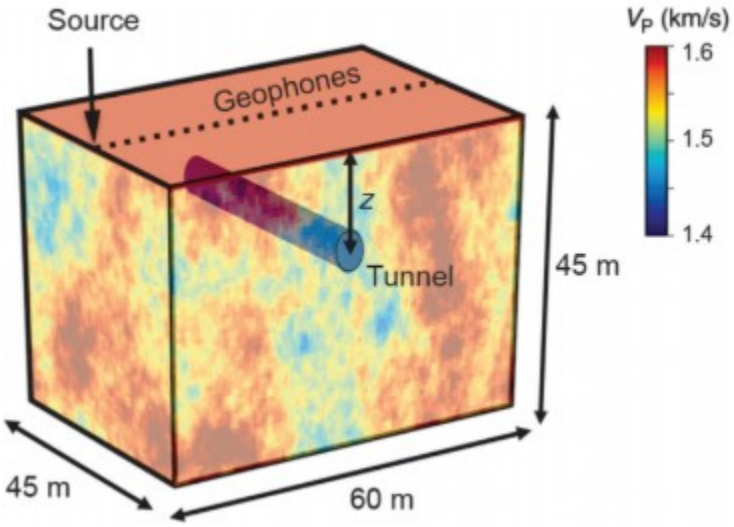

Figure 3. Block diagram showing the numerical model geometry and the location of the seismic sources and virtual geophones. In our analysis, the values of depth z are with reference to the tunnel center. The colormap is taken from a realization of the subsurface V_P, with a standard deviation of 8%.

The embedding medium is assumed to have an average V_P of 1.5 km/s, V_S of 1.0 km/s, a density of 2300 kg/m3, and a Q of 10. The heterogeneity in this medium is based on an independent realization of a fractal model in V_P, with the variability ranging up to a standard deviation of 8%, and a constant V_P/V_S ratio and density.

The target void is a cylindrical tunnel with the diameter ranging from 1.7 to 4.4 m, buried at a depth (to the center) ranging from 2 to 10 m, and filled with either water or “heavy air.” The assumption of heavy air, which has an assumed density of 1 g/cm3, V_P of 0.35 km/s, and V_S of 0 km/s, is necessary from a numerical perspective because of the very large contrast between the embedding medium and the tunnel that would require very small time steps and could introduce numerical instability into the results. To further increase the stability of the simulation, we linearly grade the material properties of the tunnel over a few grid points.

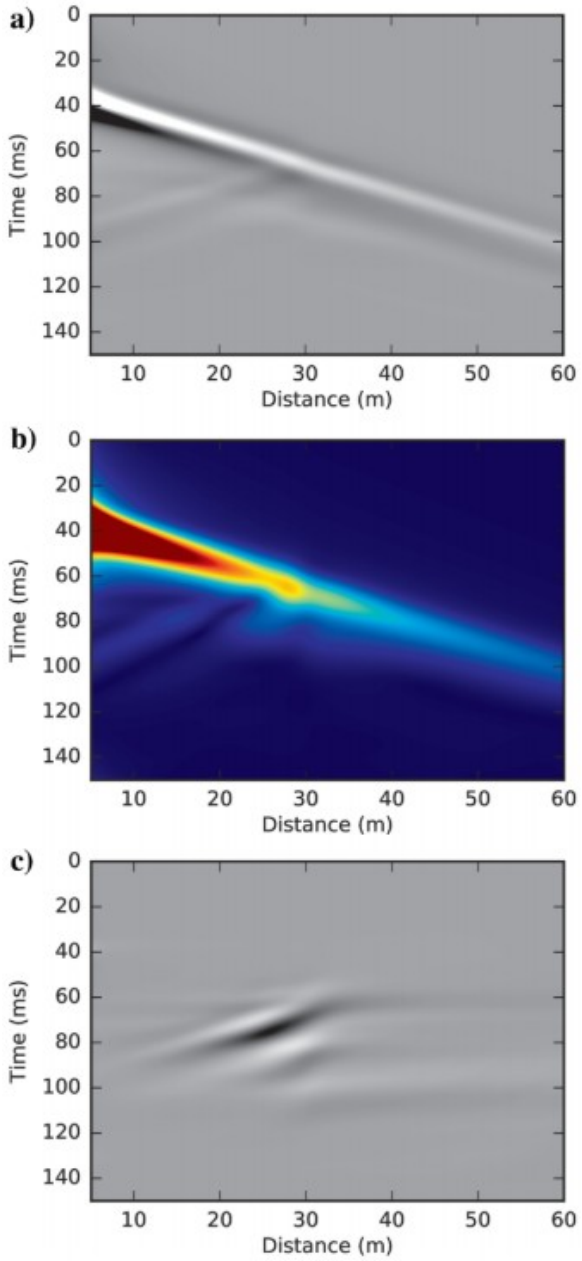

Figure 4. (a) The recorded vertical velocity field for a numerical simulation with a tunnel at a distance of 30 m, buried 4 m beneath the surface, and with a mean seismic frequency of 60 Hz, (b) the magnitude of the Hilbert envelope for the wavefield, and (c) the velocity field after applying AGC and the *f-k* filter.

A free-surface boundary condition is applied to the top of the model domain, and an absorbing boundary condition is applied to the sides and bottom of the domain. To further minimize the boundary reflection, we extend the domain boundaries outward beyond the region of interest and apply a highly attenuating material to the region adjacent to the absorbing boundaries. The seismic source is a vertical point force on the surface of the domain that is the integral of a Ricker wavelet with a nominal center frequency ranging from 30 to 100 Hz (corresponding to dominant wavelengths from 30 to 9.2

m). Because we are primarily interested in the Rayleigh wave-field, we measure the vertical and radial particle velocity along the surface of the domain perpendicular to the axis of the tunnel. The simulations were performed using the resources at Livermore Computing, and each typically required 350 cpu hours to complete.

Field survey

The seismic data at the BDM field site were collected by students at the University of California Berkeley using a set of 24 vertical spiked, 14 Hz geophones, which are damped 50%, have a flat response to 250 Hz, and were sampled at 2000 Hz. The geophones were placed in a 76 m long array perpendicular to and centered on the estimated axis of the target tunnel. Seismic sources were generated using a 20 lb sledgehammer with an aluminum plate placed on the ground at 6 m intervals along the array.

In conjunction with the linear geophone array (GA) that was designed to mirror the numerical simulation geometry, the geophones and sources were also deployed in a rectangular array around the target to collect tomographic data. In addition to the seismic data, a limited set of microgravity measurements were collected near the anticipated location of the upper tunnel using a LaCoste Romberg G meter along the axis of the linear GA.

RESULTS

Numerical study

Wavefield data

The vertical component of the simulated seismic wavefield for a simulation with a water-filled tunnel buried at a distance of 30 m and at a depth (measured to the center) of 4 m is given in Figure 4a. These data were corrected for the effects of spherical spreading, and they have a mean frequency of 60 Hz. At this level of processing, the effect of the tunnel on the surface wavefield is seen as a drop in amplitude of the direct Rayleigh phase as it passes over the tunnel axis and the backscattered Rayleigh wave originating from the same location. Because there are no apparent boundary reflection arrivals apparent in this plot, we are confident that the absorbing boundary conditions are working well and that the model domain is sufficiently large for our analysis. The corresponding Hilbert envelope function for this wavefield (Figure 4b) further highlights the variations in the surface-wave amplitude due to the tunnel. Figure 4c shows the wavefield after an *f*-*k* filter is applied to highlight the backscattered phases. The apparent source of the backscattered waves is clear in this figure, and it corresponds to the tunnel axis. In some cases, the filtering introduces small ripple artifacts into the data, which appear as vertical plane-wave arrivals.

Effect of tunnel depth and filling material

The attenuation curves for a set of water-filled tunnel simulations and the corresponding tunnel seismic anomalies for the vertical component of the

wavefield, which are calculated using equation 1 and the prescribed values of V_r and Q of the background material in the numerical simulation, are given in Figure 5. For these simulations, the diameter of the tunnels and mean seismic frequency are held constant at 1.7 m and 30 Hz (corresponding to a dominant wavelength of 30 m), whereas the depth to the center of the tunnel varies from 2 to 10 m. To verify the behavior of the numerical boundary conditions, we also simulate the equivalent tunnel-free model with the same source characteristics and background heterogeneity. We found that over the region of interest, the deviation of the reference simulation from the expected values was minor. For each of these tunnel simulations, there is a measurable pulse in the attenuation curves centered around the tunnel axis at 30 m. The peak-to- peak amplitude of the pulse tends to decrease, and the width of the pulse tends to increase as the depth to the center for the tunnel in- creases. In contrast, the static offset, which we define as the final value of the tunnel seismic anomaly at the end of the survey line, is minor for these simulations.

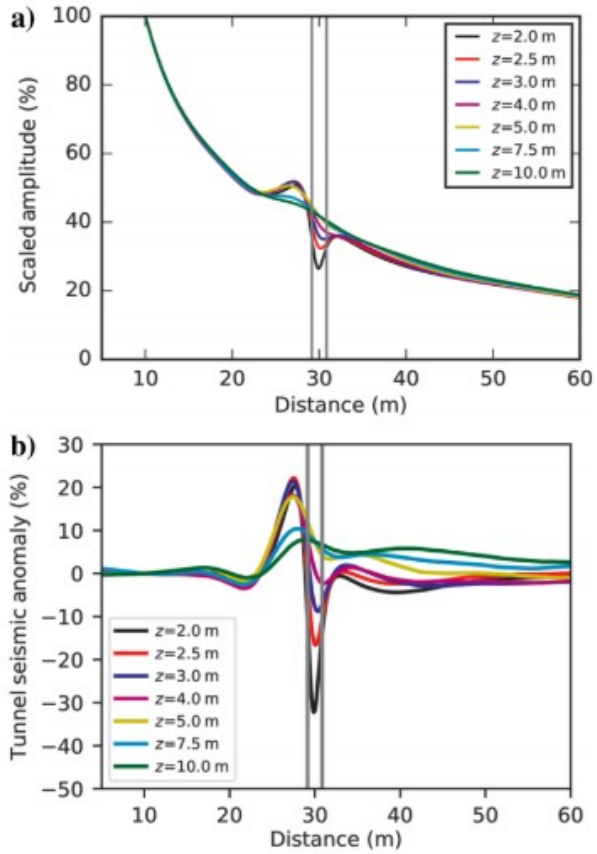

Figure 5. (a) The attenuation curves for a set of simulations containing water-filled tunnels centered at depths ranging from 2 to 10 m, with a diameter of 1.7 m and mean seismic frequency of 30 Hz (corresponding to a dominant wavelength of 30 m) and (b) the deviation of the expected attenuation curve from an equivalent tunnel-free simulation. The vertical gray lines indicate the positions of the tunnels.

The corresponding attenuation curves and tunnel seismic anomalies for a set

of air-filled tunnels, with the same source characteristics and depth range, are given in Figure 6. A comparison of the seismic anomalies and backscattered wave amplitudes between the water and air-filled simulations is given in Figure 7. In either case, the filling material in the tunnel results in a very large impedance contrast, and this leads to only a small variation in the peak-to- peak amplitude of the seismic anomaly and backscattered wave- field. Given these results, although we expect that the amplitude of the backscattered wavefield is reduced due to the use of heavy air in these models, it is not clear whether it is possible to determine whether a tunnel is filled with air or water based on surface-wave scattering or backscattering alone, especially considering other possible variations in rock heterogeneity and tunnel geometry.

In our analysis of tunnel detection methods, we focus primarily on the vertical component of the wavefield because it is much less common to measure triaxial data in the field. Because our study is primarily numerical, we are able to record the horizontal component of the wavefield at no additional cost. Instead of using equation 1 to calculate the equivalent seismic anomalies for these data, we instead consider the changes in the ratio between the total energy measured in the vertical (E_z) and horizontal (E_x) components of the wavefield. The results in Figure 8 show that E_z/E_x changes between 25% and 50% compared with an equivalent tunnel-free simulation as the wavefield passes over the tunnel axis.

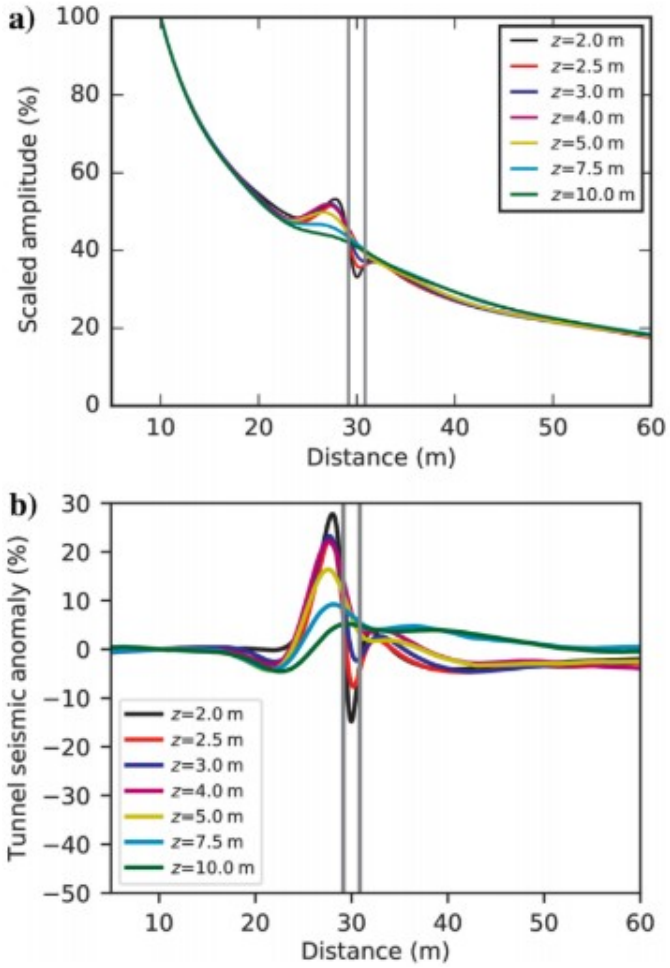

Figure 6. (a) The attenuation curves for a set of simulations containing air-filled tunnels centered at depths ranging from 2 to 10 m, with a diameter of 1.7 m and mean seismic frequency of 30 Hz, and (b) the deviation of the expected attenuation curve from an equivalent tunnel-free simulation. The vertical gray lines indicate the positions of the tunnels.

Effect of tunnel size

Holding the depth to the center of the target tunnel at 4 m and the seismic frequency at 30 Hz (dominant wavelength of 30 m), we vary the diameter of the tunnel from 2.0 to 4.0 m. The attenuation curves in Figure 9 and the correlation of the tunnel seismic anomalies with diameter in Figure 10 show that as the tunnel size increases, the backscattered wave amplitude, peak-to-peak amplitude, and static offset of the seismic anomaly increase.

Effect of seismic frequency

The attenuation curves and tunnel seismic anomalies for a set of water-filled tunnel simulations, with the depth to the center of the tunnel held constant at 4.0 m and the central frequency of the source wavelet is varied from 30 to 100 Hz (corresponding to dominant wavelengths from 30 to 9.2 m), is given in Figure 11.

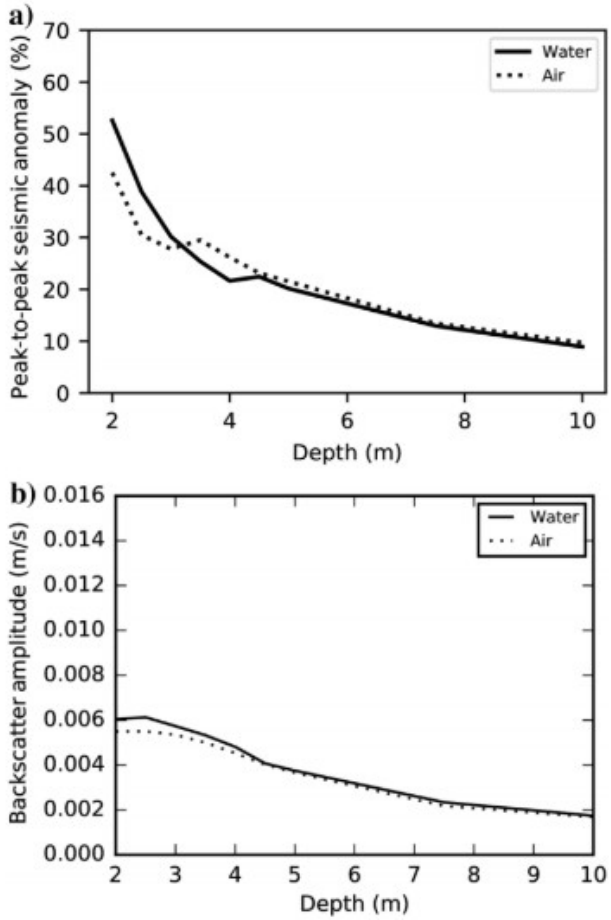

Figure 7. A comparison between the (a) seismic anomaly and (b) backscattered amplitude at 25 m from air- and water-filled tunnels, buried at depths ranging from 2 to 10 m, with a dominant frequency of 30 Hz. Because of their similarity, we do not expect to be able to determine whether a tunnel is filled with water or air based on this method alone.

As before, there is a clear pulse in the seismic anomaly for each of these simulations around the tunnel axis at 30 m; however, in some simulations there is also a static offset observed in the final seismic anomaly. Figure 12 shows that as the frequency increases, the amplitude of the static offset in the seismic anomaly and the amplitude of the backscattered arrival tend to increase, whereas the PTP remains fairly flat. There is also an increase in the noise level as the frequency increases, which is due to the interaction of the wavefield with the heterogeneous background material. Note that in each of these simulations, the tunnel is buried at a fraction of the seismic wavelength. As the dominant wavelength approaches the burial depth, at some point these signals will begin to decrease in amplitude significantly.

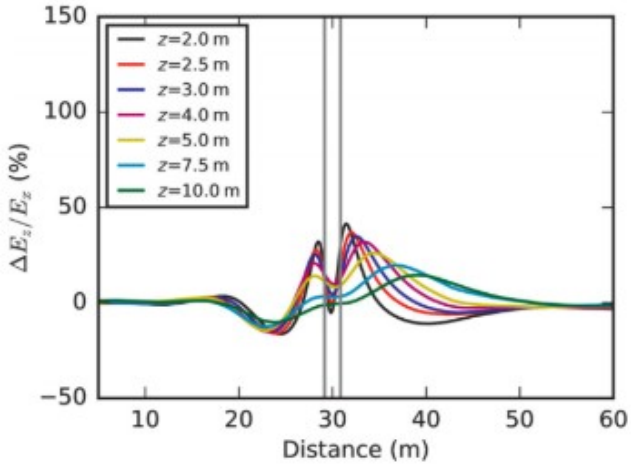

Figure 8. The ratio between the total energy recorded in the vertical and horizontal components of the surface wavefield for a set of simulations containing water-filled tunnels buried at depths ranging from 2 to 10 m, with a diameter of 1.7 m and mean seismic frequency of 30 Hz.

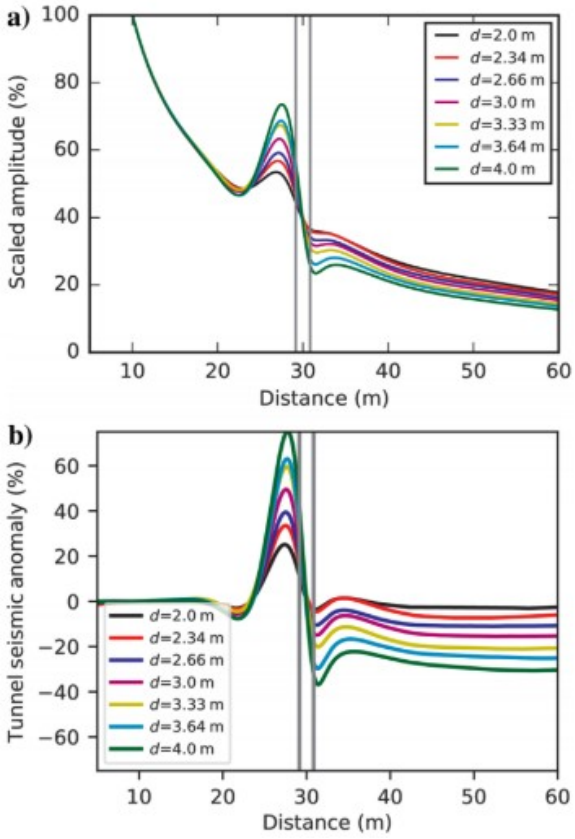

Figure 9. (a) The observed attenuation curves for a set of simulations containing air-filled tunnels buried at a depth of 4 m, with a mean seismic frequency of 30 Hz, and diameters ranging from 2 to 4 m, and (b) the deviation of the expected attenuation curve from an equivalent tunnel-free simulation.

Black Diamond Mines field study

Microgravity

The gravitational anomaly in the microgravity measurements taken along a

section of the BDM GA and the expected anomaly calculated using the standard closed-form solutions for an air-filled cylinder are given in Figure 13. These data are corrected for the Free Air and Bouguer anomalies, instrument drift, and the observed spatial trends. Although these measurements are limited, the observed anomaly agrees well with the expected depth to the center of the tunnel equal to 6.2 m and diameter of 2.8 m.

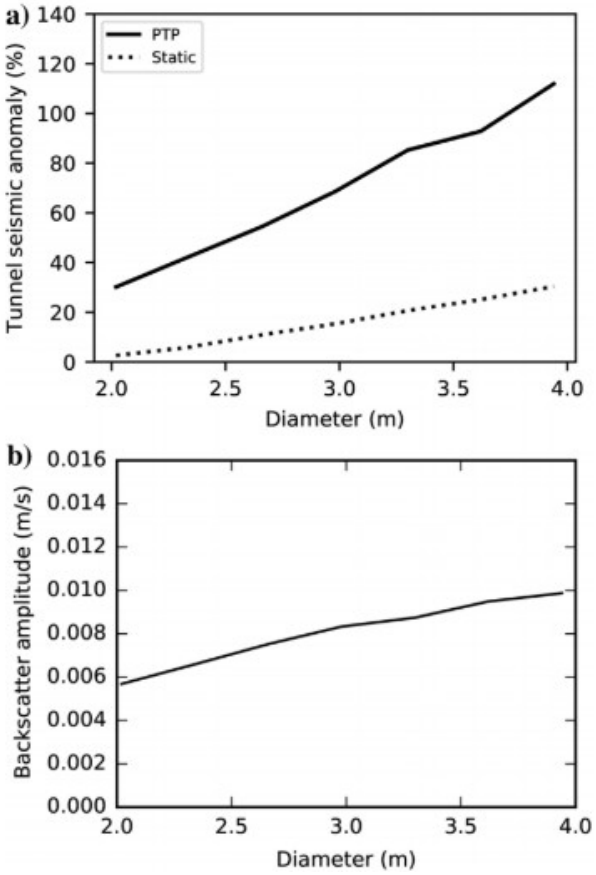

Figure 10. A comparison between the (a) peak-to-peak and static seismic anomalies and (b) backscattered amplitude at 25 m from the source for a water-filled tunnel buried at a depth of 4 m, with a seismic frequency of 30 Hz, and diameters ranging from 2 to 4 m.

Seismic data

An example of the seismic data collected at BDM and the cor- responding backscattered wavefield are given in Figure 14. These data are for a shot 76 m north of the GA, have been filtered using a bandpass of 10–20 Hz, and have been corrected for geometric spreading effects. At a distance of approximately 40 m, there is a clear discontinuity in the amplitude of the surface-wave phase and there is the source of backscattered waves.

The measured attenuation curve and the tunnel seismic anomaly for this shot are given in Figure 15. The value of Q at this site was estimated by processing data from a nearby refraction survey, which did not cross the tunnel. For reference, we also plot our assumed tunnel-free attenuation

curve, which was fit from the segments of seismic traces not crossing the expected tunnel axis and the simulated seismic anomaly for a target centered at a depth of 6.2 m with a diameter of 5.6 m. The zero crossing of the resulting tunnel pulse is located at approximately 42 m, and the peak-to-peak amplitude of the pulse is approximately 120%. The location, amplitude, and shape of these features are consistent for shots taken on the opposite side of the array; they agree with the expected location of the tunnel from historical records; and they are an excellent match for the simulated seismic anomaly.

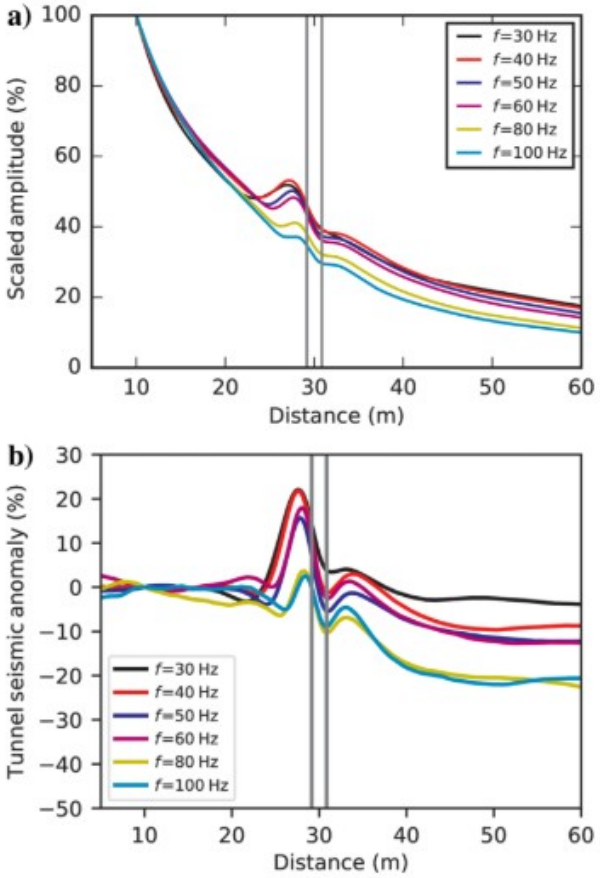

Figure 11. (a) The observed attenuation curves for a set of simulations containing water-filled tunnels buried at a depth of 4 m, with the mean seismic frequency varying from 30 to 100 Hz (corresponding to dominant wavelengths from 30 to 9.2 m), and (b) the deviation of the expected attenuation curve from an equivalent tun- nel-free simulation.

DISCUSSION

The numerical simulations presented in this paper highlight several features that may be exploited to determine the location of a buried tunnel. The static change in the surface-wave amplitude as it passes over the tunnel, which may be interpreted as a local decrease in Q, requires the fewest measurement points to observe but is typically lower in amplitude than other signals of interest. In the context of an attenuation tomography survey, we would interpret the location of the target object to be centered on the low-Q

region. Although we did not measure these data in the BDM case study, our numerical simulations suggest that changes in the ellipticity of the wavefield (Figure 8) may also be useful in identifying a tunnel in a seismic record.

In contrast, the transient pulse in the surface-wave amplitude requires a higher survey resolution to observe a tunnel of the order of 1–2 m, but it provides a more reliable and higher amplitude signal than the static offset value. In each of our simulations, the location of the zero crossing of this anomaly always corresponded to the tunnel axis. Considering the results of the tunnel depth and diameter sensitivity studies (Figures 5 and 9), there is a clear potential for nonunique interpretation of these parameters if only the amplitude of the tunnel anomaly is considered. We suggest that the best method to resolve this nonuniqueness is by using a complementary tunnel detection method such as body-wave diffraction.

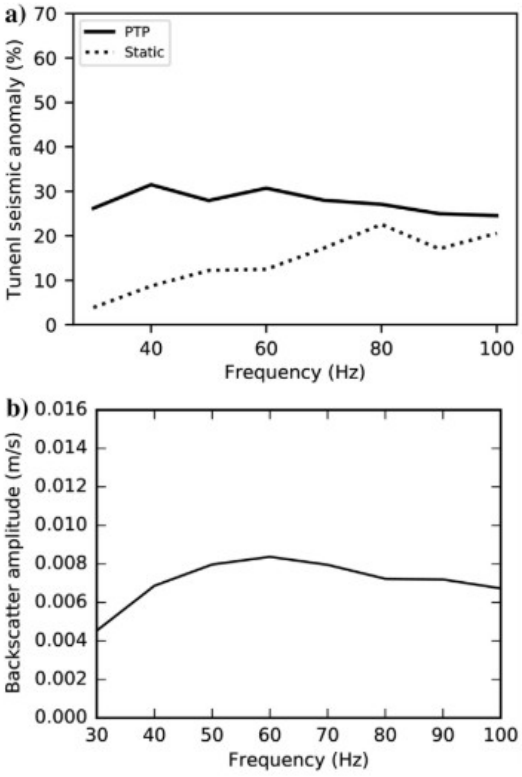

Figure 12. A comparison between the (a) peak-to-peak and static tunnel seismic anomalies and (b) backscattered amplitude at 25 m from the source for a water-filled tunnel buried at a depth of 4 m for seismic frequencies ranging from 30 to 100 Hz.

The other major signal of interest for tunnel detection is the back- scattered wavefield, which has been discussed extensively by other researchers and requires a similarly high survey resolution. As expected, we found that the apparent source of the backscattered waves corresponds to the position of the tunnel axis and that the amplitude of the backscattered wavefield was correlated with the amplitude of the pulse in the attenuation curve. To determine the depth of burial for the tunnel, other researchers have suggested using a frequency-domain analysis (Ivanov et al., 2016). We found

that the amplitude of the backscattered wavefield and the attenuation curve anomalies for an air-filled tunnel were only slightly larger than those for water-filled tunnels. This behavior was expected because, in either case, the shear velocity in the tunnel is zero and will block that portion of the energy.

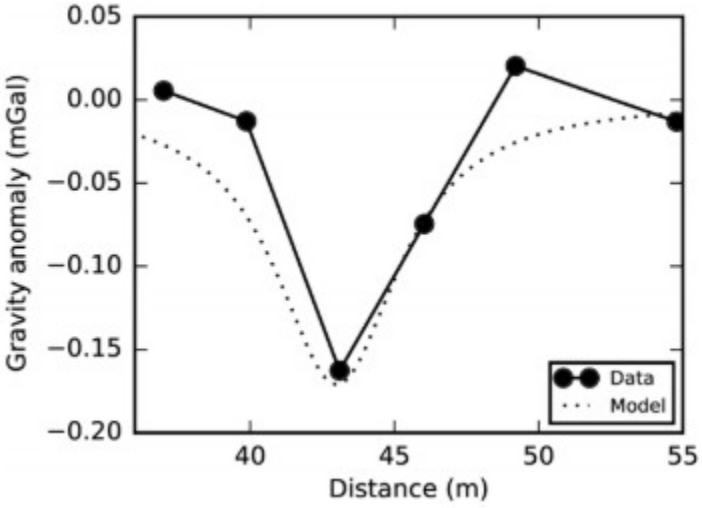

Figure 13. The observed gravitational anomaly along the BDM array compared with the expected anomaly for a tunnel located at a distance of 43 m, at a depth of 6.2m, with a diameter of 5.6 m.

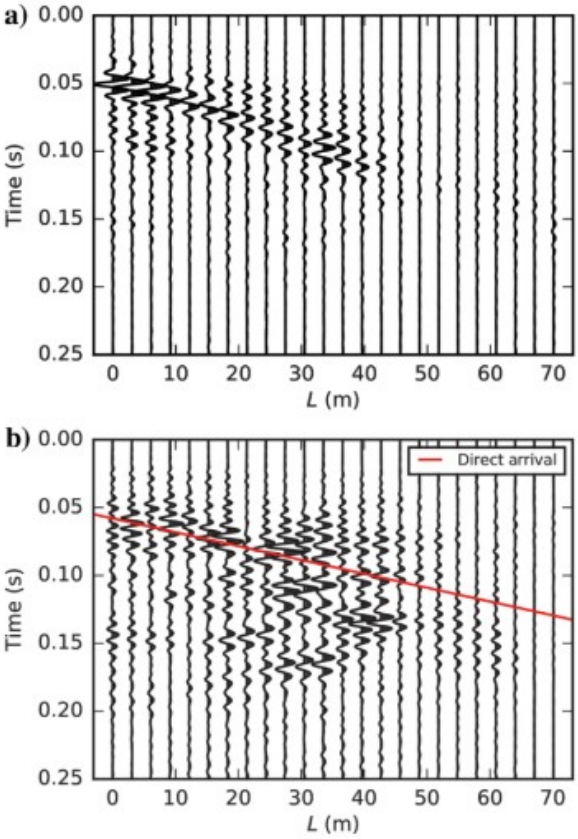

Figure 14. (a) The vertical velocity for a shot located 76 m north of the BDM GA, with a band-pass filter of 10–20 Hz. The historical records suggest that the upper tunnel is located at a distance of approximately 45 m. (b) The vertical velocity after applying the AGC *and f-k* filter. The apparent source

of the backscattered waves is at a distance of 40 m, and the expected arrival of the direct surface wave is shown in red.

Because this is primarily a numerical wave propagation study, we have not considered the effect of the method of construction and/or any support structures on tunnel detectability. Especially for large unlined tunnels, we expect there to be a zone of damage surrounding the tunnel, which would increase the amplitude of the seismic anomaly and the backscattered wavefield. In turn, this could lead to an overestimation of the true diameter of the tunnel.

To arrive at an independent estimate for the amplitude of the tunnel anomaly, we consider a simple model in which there is a total reflection or absorption of the surface wave over the target cross section. Using an exponential model for the incident surface-wave

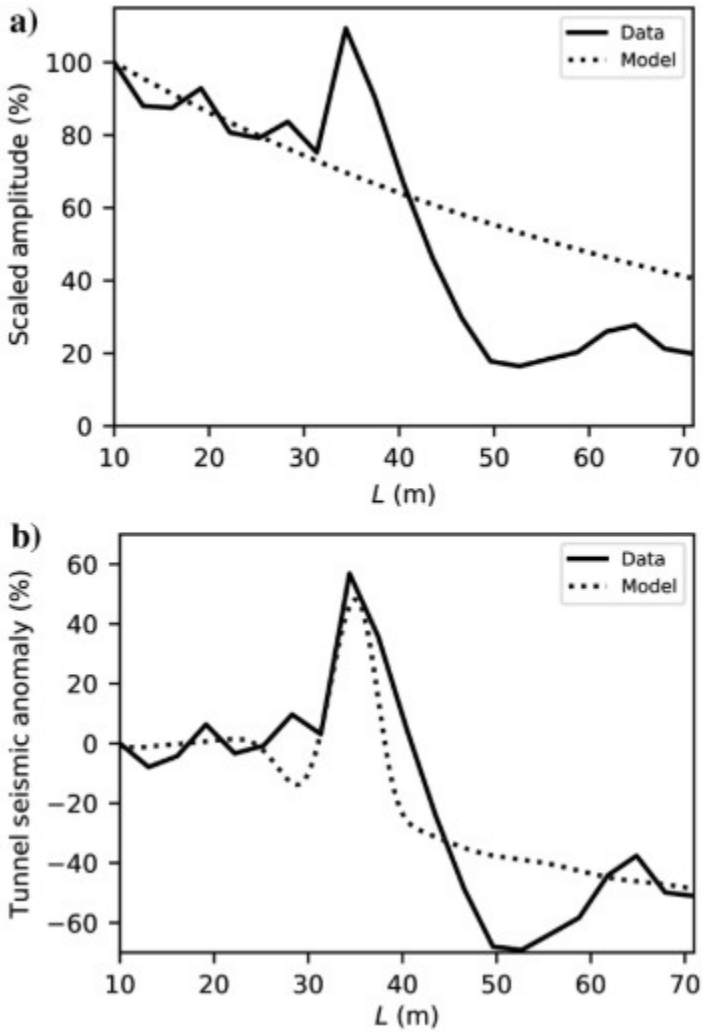

Figure 15. (a) The average attenuation curve for a set of shots on the north side of the BDM array (solid) and an equivalent tunnel-free model (dashed). (b) The measured tunnel seismic anomaly along the BDM array (solid) compared with the simulated results for the expected tunnel geometry (dashed).

energy, we estimate the expected tunnel seismic anomaly $\hat{S}$ by integrating over depth:

$$\Delta E = \int_{h-bd/2}^{h+bd/2} \exp\left(\frac{-az}{\lambda}\right) dz$$
$$= \left(\frac{2\lambda}{a}\right) \exp\left(\frac{-ah}{\lambda}\right) \sinh\left(\frac{abd}{2\lambda}\right), \qquad (2)$$

where *a* and *b* are the constants, *h* is the depth to center of the tunnel, *d* is the tunnel diameter, and λ is the wavelength of interest. Assuming a similar exponential form for the tunnel anomaly and ignoring any crossterms between tunnel depth and diameter, we find the best-fit function using the ordinary least-squares method (with $R^2 = 0.93$):

$$\hat{S} = 26.52 \exp\left(-6.85\frac{h}{\lambda} + 16.81\frac{d}{\lambda}\right). \qquad (3)$$

Assuming an overall noise level of 20% in the seismic anomaly, we may rearrange equation 3 to determine the approximate depth limit for surface-wave tunnel detection methods:

$$h < 0.041\lambda + 2.454d. \qquad (4)$$

Note that because our definition of the tunnel anomaly is a measure of the total energy of the surface wave passing through a station, thereby ignoring its phase, we expect these relationships to hold for more dispersive systems.

The mean frequency of the data considered at the BDM test site is 20 Hz, which corresponds to a wavelength of approximately 50 m. Considering the results of the regression analysis in equation 4, we would expect observe the anomaly associated with the upper (6.2 m depth, 5.6 m diameter) and lower (24 m depth, 2 m diameter) tunnels if they were buried above depths of 15 and 7 m respectively. As is clear from Figure 15, the upper tunnel is within the detection limit for the surface-wave methods and the lower tunnel is not.

CONCLUSION

The parametric numerical analysis and the case study performed at the BDM illustrate the effectiveness of surface-wave-based methods for determining the location of voids, such as man-made tunnels. We propose that these methods will locate a target if it is buried at a depth less than that given in equation 4. Because of the minimal processing involved, the time-domain methods highlighted in this paper are especially useful for determining the approximate lateral location of an object in the field and focusing efforts for higher effort and higher resolution methods such as body-wave diffraction.

ACKNOWLEDGMENTS

We would like to thank S. Larson at Lawrence Livermore National Laboratory for the use of the wave propagation code E3D. We would also like to express our thanks to J. McKana and S. Shallenberger with the East Bay Regional Parks District for providing access to the experimental site, and with the students at UC Berkeley who assisted with the fieldwork. This research was made possible by grants from the National Science Foundation, CMMI-0919595 and CMMI-0727726. Parts of this work were performed under the auspices of the U.S. Department of Energy by Lawrence Livermore National Laboratory under contract DE-AC52-07NA27344.

REFERENCES

1. Belfer, I., I. Bruner, S. Keydar, A. Kravtsov, and E. Landa, 1998, Detection of shallow objects using refracted and diffracted seismic waves: Journal of Applied Geophysics, 38, 155–168, doi: 10.1016/S0926-9851(97)00025-6.

2. Butler, D. K., 1984, Microgravimetric and gravity gradient techniques for detection of subsurface cavities: Geophysics, 49, 1084–1096, doi: 10.1190/1.1441723.

3. Ivanov, J., R. D. Miller, C. B. Park, and N. Ryden, 2003, Seismic search for underground anomalies: 73rd Annual International Meeting, SEG, Expanded Abstracts, 1223–1226.

4. Ivanov, J., R. D. Miller, and S. Peterie, 2016, Detecting and delineating voids and mines using surface-wave based methods in Galena, Kansas: 86th Annual International Meeting, SEG, Expanded Abstracts, 2344–2350.

5. Kaufmann, G., D. Romanov, and R. Nielbock, 2011, Cave detection using multiple geophysical methods: Unicorn cave, Harz Mountains, Germany: Geophysics, 76, no. 3, B71–B77, doi: 10.1190/1.3560245.

6. Korneev, V., 2009, Resonant seismic emission of subsurface objects: Geophysics, 74, no. 2, T47–T53, doi: 10.1190/1.3068448.

7. Larsen, S., and J. Grieger, 1998, Elastic modeling initiative. Part III: 3-D computational modeling: 68th Annual International Meeting, SEG, Expanded Abstracts, 1803–1806.

8. Llopis, J. L., J. B. Dunbar, L. D. Wakeley, and M. K. Corcoran, 2005, Tunnel detection along the southwest U.S. border: Presented at the Symposium on the Application of Geophysics to Engineering and Environmental Problems, 430–443.

9. Martínez-Moreno, F. J., A. Pedrera, J. Galindo-Zaldivar, S. Martos-Rosillo, L. Gonzalez-Castillo, J. P. Sanchez-Ubeda, and C. Marin-Lechado, 2013, Combined microgravity, electrical resistivity tomography and induced polarization to detect deeply buried caves: Algaidilla cave (Southern Spain): Engineering Geology, 162, 67–78, doi: 10.1016/j.enggeo.2013.05.008.

10. McCann, D. M., P. D. Jackson, and M. G. Culshaw, 1987, The use of

geophysical surveying methods in the detection of natural cavities and mine-shafts: Quarterly Journal of Engineering Geology and Hydrogeology, 20, 59–73, doi: 10.1144/GSL.QJEG.1987.020.01.06.

11. Mochales, T., A. M. Casas, E. L. Pueyo, O. Pueyo, M. T. Roman, A. Pocovi, M. A. Soriano, and D. Anson, 2008, Detection of underground cavities by combining gravity, magnetic and ground penetrating radar surveys: A case study from the Zaragoza area, NE Spain: Environmental Geology, 53, 1067–1077, doi: 10.1007/s00254-007-0733-7.

12. Morton, S., S. Peterie, J. Ivanov, R. Miller, and D. Feigenbaum, 2016, Feasibility study using surface wave attenuation and seismic quality factor for tunnel detection at the Yuma proving ground, AZ: 86th Annual International Meeting, SEG, Expanded Abstracts, 2351–2356.

13. Nasseri-Moghaddam, A., G. Cascante, and J. Hutchinson, 2005, A new quantitative procedure to determine the location and embedment depth of a void using surface waves: Journal of Environmental & Engineering Geophysics, 10, 51–64, doi: 10.2113/JEEG10.1.51.

14. Peterie, S. L., R. D. Miller, and D. W. Steeples, 2009, Diffraction imaging versus reflection processing for shallow void detection: 79th Annual International Meeting, SEG, Expanded Abstracts, 1421–1424.

15. Putnam, N. H., X. Peng, J. D. Cawlfield, O. N. Kovin, E. V. Torgashov, P. Modur, C. Stagner, S. L. Grant, N. L. Anderson, and A. Nasseri-Moghaddam, 2009, Attenuation analysis of Rayleigh waves used to locate shallow manmade tunnels: Presented at the 43rd US Rock Mechanics Symposium and 4th US-Canada Rock Mechanics Symposium.

16. Riddle, G. I., C. J. Hickey, and D. R. Schmitt, 2010, Subsurface tunnel detection using electrical resistivity tomography and seismic refraction tomography: A case study: Presented at the 23rd EEGS Symposium on the Application of Geophysics to Engineering and Environmental Problems, 552–562.

17. Rybakov, M., V. Goldshmidt, L. Fleischer, and Y. Rotstein, 2001, Cave detection and 4-D monitoring: A microgravity case history near the Dead Sea: The Leading Edge, 20, 896–900, doi: 10.1190/1.1487303.

18. Sabatier, J. M., and G. M. Matalkah, 2008, A study on the passive detection of clandestine tunnels: IEEE Conference on Technologies for Homeland Security, 353–358.

19. Sherman, C. S., J. Rector, and S. D. Glaser, 2014, The effects of near source heterogeneity on shear wave evolution: Geophysics, 79, no. 4, T233–T241, doi: 10.1190/geo2013-0199.1.

20. Sloan, S. D., J. J. Nolan, S. W. Broadfood, J. R. McKenna, and O. M. Metheny, 2013, Using near-surface seismic refraction tomography and multichannel analysis of surface waves to detect shallow tunnels: A feasibility study: Journal of Applied Geophysics, 99, 60–65, doi: 10.1016/j.

jappgeo.2013.10.004.

21. Sloan, S. D., S. L. Peterie, J. Ivanov, R. D. Miller, and J. R. McKenna, 2010, Void detection using near-surface seismic methods, in R. D. Miller, J. H. Bradford, and K. Holliger, eds., Advances in near-surface seismology and ground-penetrating radar: SEG Geophysical Developments Series 15, 201–218.

22. Sloan, S. D., S. L. Peterie, R. D. Miller, J. Ivanov, J. T. Schwenk, and J. R. McKenna, 2015, Detecting clandestine tunnels using near-surface seismic techniques: Geophysics, 80, no. 5, EN127–EN135, doi: 10.1190/geo2014-0529.1.

23. Sullivan, R., and M. D. Sullivan, 2012, Sequence stratigraphy and incised valley architecture of the Domengine formation, Black Diamond Mines Regional Preserve and the southern Sacramento Basin, California, U.S.A: Journal of Sedimentary Research, 82, 781–800, doi: 10.2110/jsr.2012.66.

24. U.S. Department of Interior, Office of Surface Mining, 1998, Manhattan Canyon Mine Subsidence: Report no. J-4382–51.

25. Van Schoor, M., 2002, Detection of sinkholes using 2D electrical resistivity imaging: Journal of Applied Geophysics, 50, 393–399, doi: 10.1016/S0926-9851(02)00166-0.

26. Vesecky, J. F., W. A. Nierenberg, and A. M. Despain, 1980, Tunnel detection: SRI International Report no. JSR-79–11.

27. Xia, J., J. E. Nyquist, Y. Xu, M. J. S. Roth, and R. D. Miller, 2007, Feasibility of detecting near-surface feature with Rayleigh-wave diffraction: Journal of Applied Geophysics, 62, 244–253, doi: 10.1016/j.jappgeo .2006.12.002.